Journal of Rock Mechanics and Geotechnical Engineering xxx (xxxx) xxx

Contents lists available at ScienceDirect

Journal of Rock Mechanics and Geotechnical Engineering

journal homepage: www.jrmge.cn

Full Length Article

Loess compaction at different water contents: Effects on hydraulic conductivity, compression behavior, microstructure, and water distribution

Kangze Yuan [a,b,c], Wankui Ni [b,*], Xiangfei Lü [b,d], Haiman Wang [b], Yongpeng Nie [b], Gabriele Della Vecchia [c,**]

[a] Department of Geology, Northwest University, Xi'an, 710069, China
[b] College of Geological Engineering and Geomatics, Chang'an University, Xi'an, 710054, China
[c] Department of Civil and Environmental Engineering, Politecnico di Milano, Milano, 20133, Italy
[d] School of Water and Environment, Chang'an University, Xi'an, 710054, China

ARTICLE INFO

Article history:
Received 12 March 2024
Received in revised form
8 February 2025
Accepted 5 March 2025
Available online xxx

Keywords:
Compacted loess
Water content
Compressibility
Hydraulic conductivity
Microstructure

ABSTRACT

In this study, compacted loess samples with varying compaction water content but identical dry density were prepared to investigate the evolution of their hydraulic conductivity and compression behavior. Additionally, environmental scanning electron microscopy (ESEM) and nuclear magnetic resonance (NMR) analyses were conducted to gain microstructural insights into loess behavior at the laboratory scale. The results indicate that the maximum saturated hydraulic conductivity is observed at the lowest compaction water content, particularly in the early stage of permeability tests. In particular, for loess compacted at water contents below the optimum (as determined by the modified Proctor compaction test), the hydraulic conductivity decreases throughout the permeability tests. Conversely, when the water content exceeds the optimum level, the hydraulic conductivity shows an increasing trend. In terms of compression behavior, when the as-compacted samples are loaded in oedometer conditions, an increase in material compressibility is observed with increasing compaction water content. Again, a different phenomenological behavior was observed when the compaction water content exceeded the optimum, i.e. an abrupt increase in loess compressibility. ESEM tests provide microstructural confirmation of this evidence, as the surface morphology of the compacted loess changes significantly with increasing compaction water content. The microstructural evolution was also quantified in terms of area ratio using image processing software. Finally, NMR was used to quantify the intra- and inter-aggregate water at different compaction water contents, once again highlighting a threshold for the presence or absence of inter-aggregate water similar to the optimum water content.

1. Introduction

Approximately 10% of the global land surface is covered by loess, mainly in arid and semi-arid regions (Yu et al., 2019). In China, the Loess Plateau, which covers approximately 640,000 km^2, is the most extensive loess deposit in the world (Hou et al., 2020). With the rapid development of China's western region, there has been a substantial increase in construction activities on the Loess Plateau in the 21st century (Hou et al., 2024). Loess is widely used in civil engineering for foundations, subgrade and embankments due to its low cost and easy availability (Wang et al., 2025). It is characterized by a distinctive particle size distribution, consisting predominantly of fine-grained particles such as silt and clay. Under dry conditions, these particles interlock to form a stable, cohesive structure that is further strengthened by cementation bonds (Li et al., 2022; Ying et al., 2023).

* Corresponding author.
** Corresponding author.
E-mail addresses: niwankui@chd.edu.cn (W. Ni), gabriele.dellavecchia@polimi.it (G. Della Vecchia).

Peer review under responsibility of Institute of Rock and Soil Mechanics, Chinese Academy of Sciences.

https://doi.org/10.1016/j.jrmge.2025.03.054

However, loess is very sensitive to water, the penetration of which into the pore space leads to a weakening of the strength of the cement and thus of the entire soil (Luo et al., 2018). Meanwhile, the high porosity of loess also provides the conditions for the metastability of the loess structure. Water intrusion can not only reduce the strength of loess but also cause the volumetric collapse of the loess structure upon wetting, with relevant implications for human life and infrastructure stability (Leng et al., 2018). Other common geological hazards in loess areas include landslides, mudflows, and subsidence, all of which are associated with water infiltration into loess (Damiano et al., 2017; Li et al., 2025).

To meet construction requirements, stabilization techniques are often used to improve the mechanical properties of loess. In addition to the classical procedures based on the improvement of the mechanical properties of the site material by means of compaction or dynamic tamping (e.g. Evstatiev, 1988; Peng et al., 2017; Yuan et al., 2024), it is also worth mentioning the availability of techniques based on the combination of the soil with certain binders. Among the various binder-based stabilization methods (Cui et al., 2018; Yuan et al., 2023), the addition of lime and cement is the most widespread due to their cost-effectiveness and proven technical efficiency (Jia et al., 2019; Ying et al., 2021a).

In recent years, there has been an increase in research on the hydromechanical properties of compacted loess due to the growing use of loess as a foundation material in construction projects worldwide (Li et al., 2016; Lan et al., 2023; Xiong et al., 2024). Given the importance of water movement in loess, hydraulic conductivity is recognized as one of its critical geotechnical properties (Chapuis, 2012; Li et al., 2024). Numerous studies have investigated the factors influencing the saturated hydraulic conductivity of loess. For example, Xu et al. (2021) reported that higher temperatures lead to an increase in the initial saturated hydraulic conductivity, while Yuan et al. (2021) highlighted the effects of wetting-drying cycles and compacted dry density. In addition, Atashgahi et al. (2020) investigated the potential of microbially induced calcite precipitation (MICP) to reduce loess permeability, and Liu et al. (2020) highlighted the critical role of compaction water content. Recent evidence also shows that saturated hydraulic conductivity evolves due to changes in pore structure driven by water infiltration (Xu et al., 2022). The magnitude of volumetric collapse is also highly dependent on material compressibility, as evidenced by several experimental data and modeling approaches that have proven successful for compacted soils (e.g. Alonso et al., 1990; Della Vecchia et al., 2013; Musso et al., 2024). To date, the compressibility of loess has been extensively studied, with research focusing on its dependence on factors such as particle size, dry density, water content, wetting-drying cycles, and freezing-thawing cycles (e.g. Mu et al., 2020; Yuan et al., 2022). However, the majority of studies have focused on the effects of water content on hydraulic conductivity and compressibility within a narrow range of intermediate compaction water contents. Investigations at the extremes, such as higher (near-saturated) and lower (near-dry) compaction water contents, remain relatively scarce.

In this context, this study analyzes the water distribution in compacted loess as a fundamental factor influencing its hydromechanical properties in the full saturation range, i.e. from dry to saturated conditions. Compacted loess samples were prepared by static compaction at different compaction water contents and the same dry density. The influence of water content on the saturated hydraulic conductivity and the unsaturated compression behavior was investigated. Subsequently, environmental scanning electron microscopy (ESEM) and nuclear magnetic resonance (NMR) tests were performed to provide a microstructural interpretation of the variations in hydraulic conductivity and compression behavior of the loess. In particular, the role of intra- and inter-aggregate water during compaction is investigated based on the distinction between intra- and inter-aggregate pores obtained by ESEM photomicrographs and according to the results of NMR, which in recent years has provided an innovative approach to the study of water distribution and water mobility in porous media (Cheng and Heidari, 2017). To further evaluate the evolution of the microstructure, an image processing software was adapted to identify the area ratio of the pores.

The significance of this study lies not only in the specific experimental results related to the specific compaction conditions, but also in the development of a comprehensive experimental framework for the interpretation of both laboratory and microstructural data in a wide range of water contents, from dry to near-saturated conditions. Although in this study the samples were prepared by static compaction, the presented methodology allowed the identification of a threshold compaction water content, almost coinciding with the optimum water content (w_{opt}) obtained by the modified Proctor test, which acts as a delimiting water content for the presence or absence of inter-aggregate water in compacted loess. The same compaction water content is related to phenomenological changes in hydraulic conductivity and material compressibility. This information can be used to select an appropriate water content during in situ compaction processes, with relevant engineering implications in all applications where loess is used as a foundation material.

2. Study area and soil properties

The study area is located in Yan'an City, near the center of the Loess Plateau. Yan'an is one of the largest cities on the plateau, characterized by a high population density and limited flat land. The region experiences a warm temperate climate with four distinct seasons, and an annual precipitation ranging from 0.52 m to 0.55 m, most of which occurs during heavy rains from June to September (Zhuang et al., 2017). The susceptibility of the area to landslides is attributed to the loose loess texture, jointed structure, and significant human activity (Zhang and Liu, 2010). The studied soil was Q_3 loess, commonly referred to as Malan loess in China, and was sampled from a depth of 7–7.5 m below the surface. Cylindrical samples, approximately 0.1 m in diameter and 0.2 m in height, were carefully extracted, sealed with paraffin, and packed in wooden boxes filled with straw to prevent disturbance during transport (Shao et al., 2018). Upon arrival at the laboratory, the physical properties of the loess were analyzed according to ASTM standards (ASTM D4318–00, 2000), and the results are summarized in Table 1. As shown in Fig. 1a, the analysis of the particle size distribution (PSD) revealed that silt constitutes the predominant composition, accounting for 75.46% of the total, while sand and clay account for 13.39% and 11.15%, respectively (GB/T 50123–2019, 2019). Based on its composition, the loess is classified as sandy clayey silt (Shepard, 1954). Mineralogical analysis conducted using X-ray diffraction (XRD) (Fig. 1b) identified the clay mineral contents (weight percent, w_t) using semi-quantitative methods (Moore and Reynolds, 1997). The results are presented in Table 2.

3. Experimental procedures and methods

3.1. Test samples

After the loess was collected, it was crushed using a wooden hammer to break up all aggregates, sieved through a 2 mm mesh, and oven-dried at 105 °C for 8 h. The compaction characteristics of the material were determined using the modified Proctor compaction test, a standard method for establishing the

Table 1
Physical properties of loess.

Natural water content (%)	Solid specific gravity	Plastic limit, w_P (%)	Liquid limit, w_L (%)
10	2.71	16.1	28.9

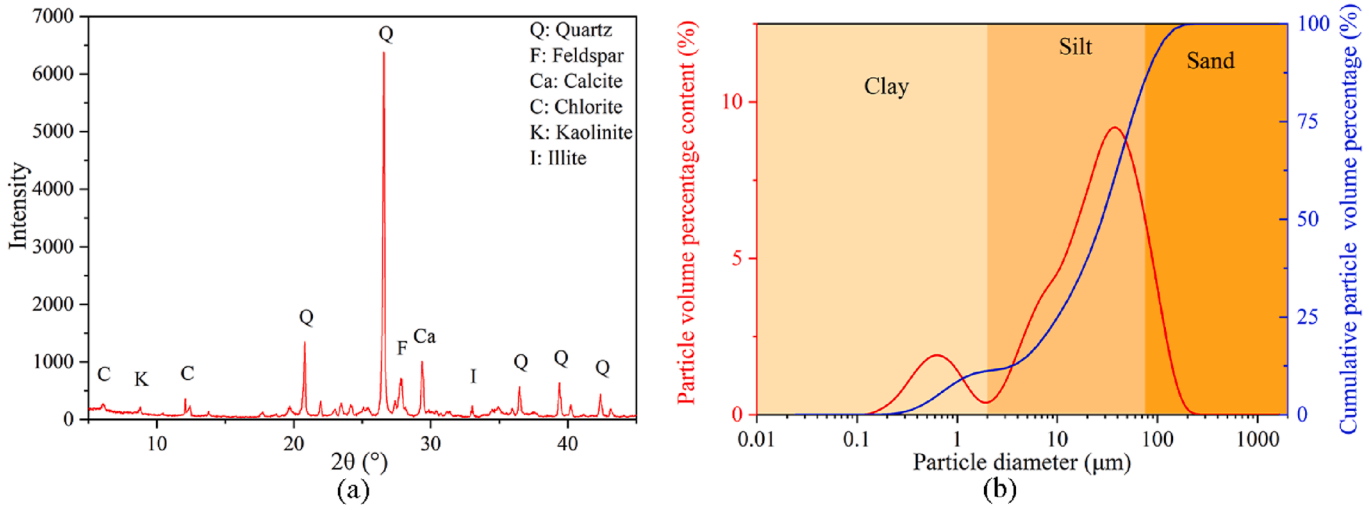

Fig. 1. (a) PSD curves; and (b) XRD pattern.

Table 2
Mineralogical composition of loess.

Mineral	w_t (%)
Quartz	45.2
Feldspar	21
Calcite	15.5
Chlorite	8
Kaolinite	5.8
Illite	4.5

relationship between compaction water content and dry density. Following ASTM D1557–00 (2000) guidelines, compaction was performed in a cylindrical metal mold with a capacity of 2.0139×10^{-3} m^3 and an internal diameter of 0.1524 m. A 4.5 kg rammer, dropped from a height of 457 mm, was used to compact the loess in five layers, with each layer receiving 56 blows, resulting in a compaction energy of 2700 kJ/m^3. The experimental results, including the black data points, along with the identification of the optimum water content (w_{opt} = 14%) and the maximum dry density (MDD = 1.74 Mg/m^3), are presented in Fig. 2 within the compaction plane. These parameters represent the specific conditions of the compaction method adopted.

Deionized water was sprayed gradually onto the samples using a spray bottle to achieve the target water content. The target water contents selected for this study were 3%, 5%, 7%, 10%, 12%, 14%, 16.1%, 19%, 22%, 25%, and 28.9%. After wetting, the samples were sealed in plastic film and placed in a humidity chamber at 25 °C for 48 h to ensure uniform water distribution. Since dry density is a key parameter influencing the quality of compacted loess in construction, the target dry density (ρ_d = 1.55 Mg/m^3), which reflects typical field conditions in the study area (Nie et al., 2024), was adopted for all samples. This corresponds to a void ratio of 0.748. The samples were statically compacted to the target density using a three-axis compactor and shaped into molds suitable for the respective tests. The degrees of saturation corresponding to the target water contents were 10.8%, 18.1%, 25.4%, 36.2%, 43.5%, 50.7%,

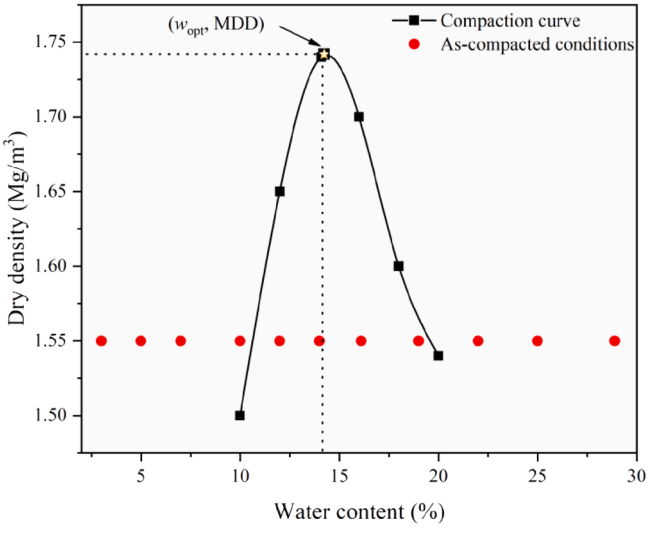

Fig. 2. Compaction curve and states corresponding to as-compacted conditions.

58.3%, 68.8%, 79.7%, 90.6%, and 100%, respectively. Cylindrical samples measuring 61.8 mm in diameter and 40 mm in height were prepared for permeability tests. Oedometer samples, 79.8 mm in diameter and 20 mm in height, were used for compression tests. The compaction plane in Fig. 2 contains the red dots, which represent the as-compacted states of the samples under the specified conditions.

3.2. Permeability testing

The samples were subjected to a variable head permeability test according to ASTM D1586–08 (2008). Fig. 3 shows the experimental setup. The TST-55 permeameter is a soil permeability and water content measuring device (Chen et al., 2023a). It is a convenient and accurate soil testing apparatus that is widely used

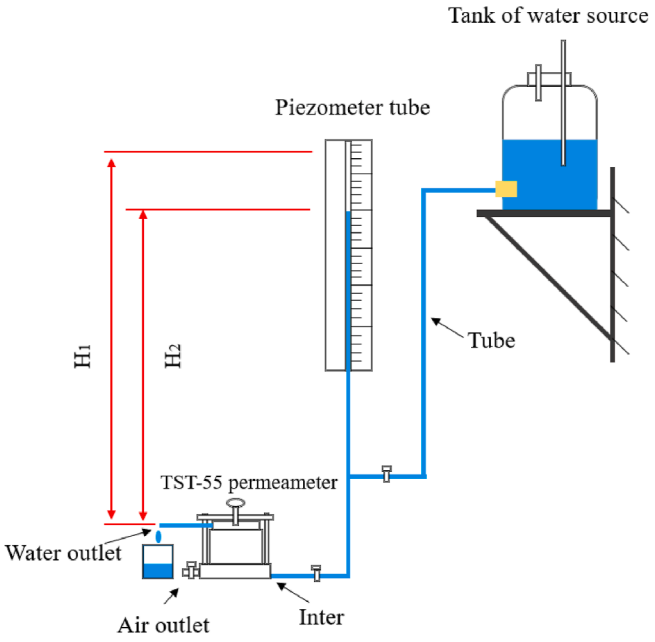

Fig. 3. Schematic of the permeability test apparatus.

in various engineering and construction fields. All samples were saturated before being processed for permeability tests. The soil samples were saturated using the variable head method, which ensured a controlled and gradual saturation process. The specific saturation test procedure was described in Xu et al. (2020). Data analysis was performed by considering the mean hydraulic conductivity values calculated for each sample using six different initial heads. The experiments were conducted under controlled conditions, maintaining an environmental temperature of 20 °C. The variable head saturated hydraulic conductivity k_T (m/s) was evaluated as

$$k_T = \frac{2.3aL}{A(t_2 - t_1)} \log_{10} \frac{H_1}{H_2} \tag{1}$$

where H_1 and H_2 are the hydraulic heads (m) at times t_1 and t_2, respectively; a is the cross-sectional area of the tube (m^2); A is the cross-sectional area of the cutting ring (m^2); L is the height of the sample (m); and t_1 and t_2 are the start and end times (s) of the head measurement, respectively.

3.3. Oedometer test

Samples were placed in an oedometer to perform oedometer tests, applying the vertical stresses in a sequence of 12.5 kPa, 25 kPa, 50 kPa, 100 kPa, 150 kPa, 200 kPa, 300 kPa, 400 kPa, 600 kPa, and 800 kPa. The compression curve, expressed in terms of void ratio (e) and total vertical stress (σ_v), was derived from the measured vertical displacement and the initial void ratio (Lei et al., 2020). The analysis focused on the evolution of preconsolidation pressure (σ_p) and compression index (C_C) over different compaction water contents. The preconsolidation pressure was determined using the well-established Casagrande procedure, while the compression index was calculated as $C_c = -\Delta e/\Delta \log \sigma_v$, which represents the slope of the virgin compression line.

3.4. ESEM analysis

Cubic sticks of approximately 10 mm × 10 mm × 20 mm (length × width × height) were taken from the center of the samples for ESEM examination. The microstructure of the sample was examined on a new surface created by breaking the soil sticks at a height of about 10 mm. Subsequently, an electron-conducting tape was used to affix the stick halves onto the sputtering pad, and platinum (Pt) coatings were sputtered in a plasma sputtering apparatus without disturbing the broken surface. ESEM was utilized to capture microstructure photographs of samples at different water contents. In this study, a series of ESEM observations were made at various positions on the samples to capture representative microstructural features and to facilitate the selection of repeatable results for presentation. This approach serves to mitigate the potential influence of local variations or biases that may manifest during the ESEM imaging process. The introduction of randomness and repeatability into the experimental design is intended to mitigate subjective influences and thus to increase the reliability of ESEM observations. In this study, an image processing software (Image-Pro Plus, IPP) was employed to quantify the microstructural evolution (see, for example, the works of Xu et al. (2021) and Li et al. (2019), among others, for details).

3.5. NMR testing

The geophysical NMR method was used to investigate the pore size distributions in loess samples, using a MacroMR12-150H-1 device. The samples were placed in the NMR device to identify the T_2 curve distribution of the samples, which can be obtained from the following equation (Kong et al., 2018):

$$\frac{1}{T_2} = \frac{1}{T_{2B}} + \frac{1}{T_{2S}} + \frac{1}{T_{2D}} \tag{2}$$

where T_{2S} is the surface-enhanced relaxation time at the pore walls, T_{2B} is the bulk water relaxation time, and T_{2D} is the diffusion relaxation time. The effects of T_{2B} and T_{2D} during the analysis are minor and ignored, as suggested by Tian et al. (2014). Therefore, the following equation can be obtained:

$$\frac{1}{T_2} = \frac{1}{T_{2S}} = \rho \frac{S}{V} = \rho \frac{\alpha}{r} \tag{3}$$

where ρ is the surface relaxivity coefficient (generally expressed in μm/s), S is the pore surface area, V is the pore volume, r is the pore radius, and α is a geometry factor. In this study, Eq. (3) is considered to be valid for both saturated and unsaturated conditions, and provides information only about the pores where water is present, i.e. the smallest pore in near-dry conditions and the entire pore space in near-saturated conditions. Since the real pore topology is very complex, for the sake of simplicity and to avoid introducing arbitrary assumptions that may complicate the interpretation of the experimental results, the pore topology was assumed to be cylindrical, regardless of the pore size (i.e. $\alpha = 2$), as widely accepted in the relevant literature (Kong et al., 2018; Tian et al., 2018; Yuan et al., 2022). Consequently, Eq. (3) finally reads

$$\frac{1}{T_2} = \rho \frac{\alpha}{r} = \rho \frac{2}{r} \tag{4}$$

or

$$T_2 = \frac{1}{2\rho} r \tag{5}$$

The Schlumberger-Doll research (SDR) equation, introduced by Kenyon et al. (1988), provides a mathematical framework for describing the relationship between NMR signals and permeability in porous media. The SDR equation relates the surface relaxivity

coefficient (ρ) to the soil saturated permeability (k_s), which is expressed as follows:

$$k_s = C\varphi^4 T_{2LM}^2 \tag{6}$$

where the constant $C = \rho^2$, φ is the porosity, and T_{2LM} is the geometric mean value of the T_2 distribution. The dependence of k_s on ρ can be expressed as

$$k_s = \rho^2\varphi^4 T_{2LM}^2 \tag{7}$$

thus, the surface relaxivity coefficient can be obtained as

$$\rho = \sqrt{\frac{k_s}{\varphi^4 T_{2LM}^2}} \tag{8}$$

4. Experimental test results

4.1. Saturated hydraulic conductivity

A series of permeability tests were performed to investigate the influence of compaction water content on the saturated hydraulic conductivity of compacted loess. The compaction water content significantly influences the initial microstructure of loess samples, exhibiting divergent effects compared to those induced by changes in the current water content in samples prepared in the same way, as shown, for example, by Sun et al. (2023) and Chen et al. (2014). For the sake of clarity, but without losing the generality of the conclusions, not all the experimental results of the evolution of the hydraulic conductivity with time are shown in Fig. 4a. As demonstrated in Fig. 4a, the results indicate distinct temporal trends in hydraulic conductivity based on the compaction conditions of the samples. In region A, which represents the initial stage of the permeability tests, the hydraulic conductivity decreases significantly with increasing compaction water content. This observation is consistent with the findings of Guo et al. (2021), who investigated the effects of four compaction water contents (6%, 10%, 14%, and 18%) on the hydraulic conductivity of loess and reported a gradual decrease in hydraulic conductivity with increasing compaction water content. However, the findings of this study show that when the compaction water content is greater than w_{opt} (as shown in Fig. 4b, where the data are collected from all experiments), the change in initial hydraulic conductivity becomes relatively less significant. Beyond w_{opt}, changes in the compaction water content appear to significantly affect the initial hydraulic conductivity. The optimum water content w_{opt} represents a threshold compaction water content in terms of the time evolution of hydraulic conductivity. In the presence of continuous water flow, when the compaction water content is lower than w_{opt} (14%), the hydraulic conductivity decreases with time. The most significant change in hydraulic conductivity over time is observed when the compaction water content reaches 3% (corresponding to a reduction in k_T of approximately 42%). As the compaction water content increases, the rate of decrease in hydraulic conductivity is reduced. For example, at a compaction water content of 14%, the hydraulic conductivity decreases from 1.2×10^{-7} m/s to 8.8×10^{-8} m/s, representing a 27% reduction. Conversely, when the compaction water content exceeds w_{opt}, the hydraulic conductivity begins to increase with time. For example, at a compaction water content of $w = 16.1\%$, the hydraulic conductivity increases from 6.49×10^{-8} m/s to 8.17×10^{-8} m/s, corresponding to a 25.8% variation. As the compaction water content increases, the time dependence of the hydraulic conductivity also increases. For example, for a compaction water content close to the saturated one, the hydraulic conductivity increased from 1.24×10^{-8} m/s to 2.55×10^{-8} m/s, corresponding to a 105.9% increase. This finding seems to differ from the results of Li et al. (2022), who investigated the hydraulic conductivity at five specific water contents (14%, 16%, 18%, 20%, and 22%) and observed an increase in hydraulic conductivity with time for loess samples. The discrepancy can be attributed to the fact that the study by Li et al. (2022) did not examine water contents below 14%, thus failing to account for potential variations in hydraulic conductivity at lower water contents. The present study addresses this gap by including and analyzing samples with water contents below 14%, thereby providing a more comprehensive understanding of the hydraulic conductivity behavior over a wider range of water contents. Since the hydraulic properties of loess are influenced by its microstructure, the fact that the hydraulic conductivity of the samples with compaction water contents up to w_{opt} tends to decrease,

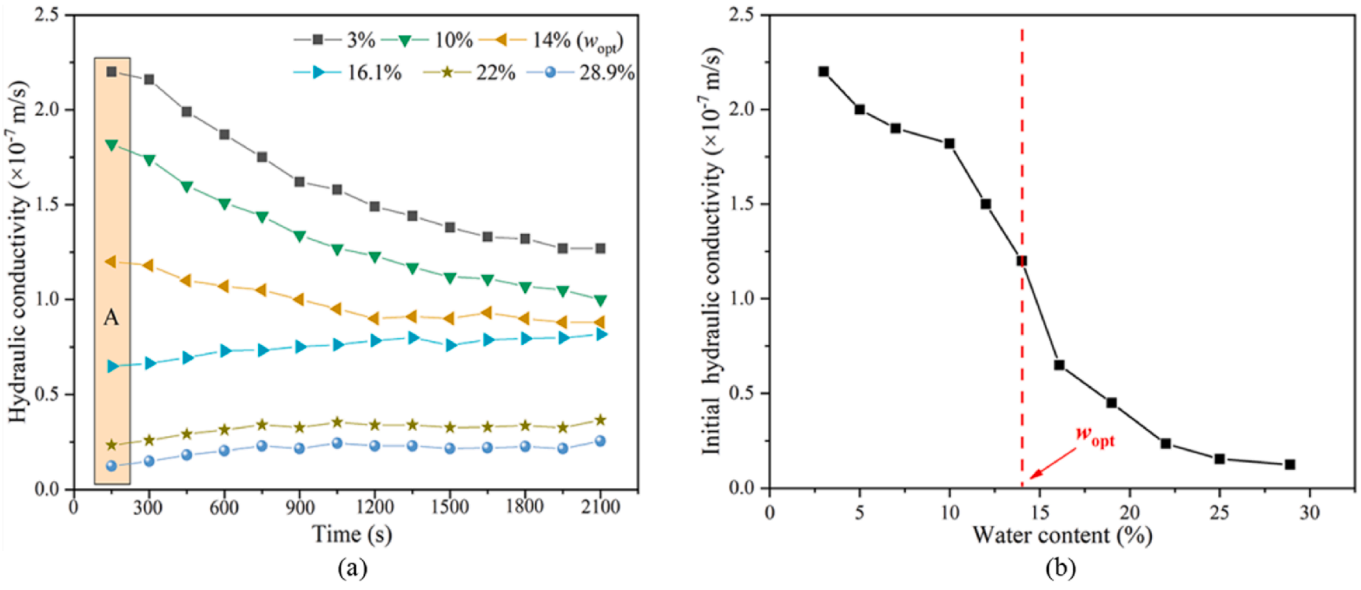

Fig. 4. (a) Time variation of the hydraulic conductivity for different compaction water contents; and (b) Evolution of initial hydraulic conductivity with compaction water content.

while the opposite is true for samples with compaction water content larger than w_{opt} suggests that microstructural changes induced by compaction are particularly relevant in a range of compaction water contents around w_{opt}.

4.2. Compression behavior

As discussed in Section 4.1, the compaction water content is critical in shaping the microstructure of loess, especially during the sample preparation processes used in this study. To illustrate the influence of compaction water content and the associated microstructural changes induced by compaction, the oedometer compression curves for loess samples prepared at different water contents are shown in Fig. 5a. Again, for clarity, not all experimental compression curves are shown in the figure. The samples were not saturated before testing, and the tests were performed by keeping the drainage lines open during compression (but water content changes were not measured throughout the compression stage).

The compression curve for the saturated loess sample ($w = 28.9\%$, black line) shows a preconsolidation pressure of 89 kPa and a normal compression line slope (C_C) of 0.0388. Consistent with the observations for non-active geomaterials, the preconsolidation pressure decreases with increasing compaction water content due to reduced matric suction, while the compression index increases, as shown in Fig. 5b. Conversely, when the vertical stress is below the preconsolidation pressure, the slope of the compression curve, referred to as the reloading index (C_R), remains relatively unaffected by water content. For samples with compaction water contents below the optimum ($w_{opt} = 14\%$), the compression curves show little variation across varying water contents. However, for water contents above w_{opt}, the compressibility of loess is significantly affected, indicating a stronger dependence on water content. A comparison of these results with those of Leng et al. (2021), who performed oedometer tests on similarly compacted loess samples with varying water contents, reveals a similar trend. However, Leng et al. (2021) reported a smoother evolution of stiffness with water content, emphasizing the critical influence of the initial microstructure on the compressibility behavior of loess. Consistent with the evidence provided by the findings of the permeability testing, the most relevant change in the compression index is identified when the compaction water content exceeds w_{opt}, again suggesting a relevant microstructural change in this compaction water content range.

4.3. Morphology of compacted loess

ESEM observations were performed to analyze the microstructural fabric of loess compacted at different water contents (Ni et al., 2020). As illustrated in Fig. 6, the images show distinct aggregations of loess particles. These observations highlight not only the presence of aggregates and inter-aggregate pore spaces (P1) but also the intra-aggregate pores (P2), consistent with the findings of Yuan et al. (2022). Aggregates are structural units formed by the aggregation of elementary soil particles (clay, silt, and sand) under the influence of various forces, including capillary forces, cementation processes, van der Waals attraction, and other interparticle interactions. These aggregates can be categorized into clay-silt and clay aggregates, with the latter being smaller in size and mostly originating from physico-chemical interactions (Xie et al., 2018). The aggregates and the pores within them form the so-called microstructural domain, also known as an intra-aggregate pore space. The inter-aggregate pore space consists of the voids between the aggregates and serves as the macrostructure (e.g. Romero et al., 2011; Musso et al., 2020; Scelsi et al., 2021). For samples with compaction water content up to the optimum water content w_{opt} (i.e. $w \leq 14\%$), the change in surface morphology with water content is very limited, and a large number of inter-aggregate pores are present in all samples. When the water content exceeds w_{opt} ($w = 16.1\%$), the number of inter-aggregate pores seems to decrease. When a higher compacted water content is considered (e.g. $w = 28.9\%$), the surface morphology of the samples changes again. Since ESEM provides only qualitative insights into the surface morphology of the samples, the evolution of pores in compacted loess at different water contents was further quantified using the image processing software IPP 6.0. This allowed for a detailed analysis of pore characteristics and their variation with compaction water content.

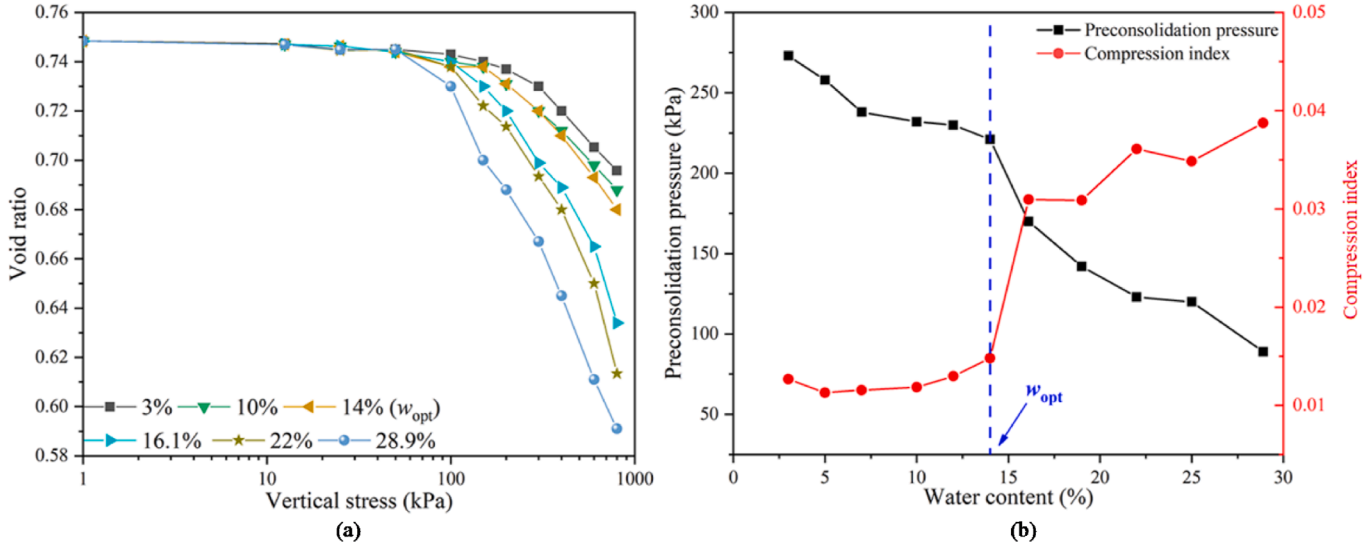

Fig. 5. (a) Compression curves; and (b) Variations of preconsolidation pressure and compression index with compaction water content.

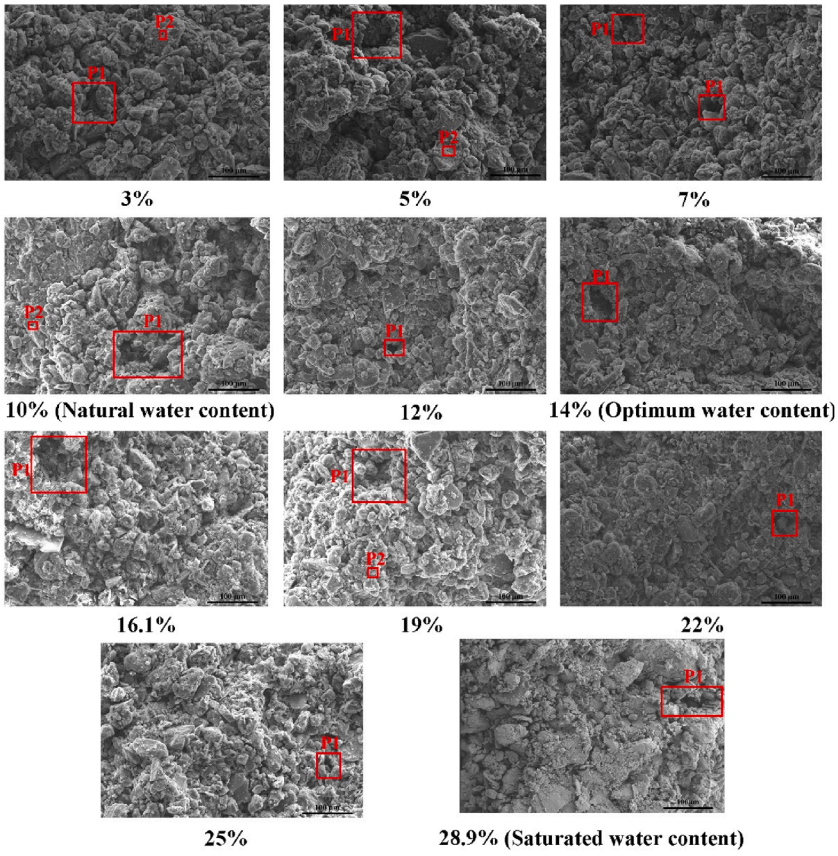

Fig. 6. ESEM images of compacted loess at different compaction water contents.

4.4. Pore area distribution

The IPP 6.0 software facilitates quantitative analysis by comparing the void fraction to the total area captured in the ESEM images, thereby enhancing the interpretation provided by visual inspection (Yuan et al., 2023). The pore area ratio (PAR), which quantifies the proportion of pore space in the observed area, is calculated as follows:

$$PAR = \frac{A_{\text{totalpore}}}{A_{\text{total}}} \times 100\% \tag{9}$$

where $A_{\text{totalpore}}$ is the total pore area, and A_{total} is the area of the ESEM image. The ability of the IPP software to assess the pore evolution was demonstrated by its ability to provide a total porosity of 41.08%, which is comparable to the porosity of the as-compacted material (42.8%) in the loess sample compacted at a water content of 3%. Loess pores are usually classified into four types based on their diameters: micropores (0–2 μm), small pores (2–8 μm), mesopores (8–32 μm), and macropores (>32 μm) (Lei, 1988). For the compacted loess at different water contents, Fig. 7 shows the ratios of the total pore area and the percentages of the four pore types calculated using the IPP program on the images in Fig. 6. Since all samples were compacted to the same dry density, the total pore area ratio remains relatively stable with increasing water content. However, as discussed in Section 4.3, the increase in water content induces the movement of clay particles within the compacted loess. This process promotes the adhesion of clay particles around aggregates, resulting in a decrease in the proportion of macropores and an increase in the proportion of mesopores. This trend is clearly illustrated in Fig. 7, which shows a decrease in the macropore area ratio and a corresponding increase in the mesopore area ratio with increasing water content.

4.5. Water distribution

The NMR curves illustrating the T_2 distribution of loess samples with different compaction water contents are shown in Fig. 8a. The results show a unimodal T_2 distribution for all samples, predominantly in the range of 0.026–38.72 ms. For the samples compacted at low water content, the T_2 relaxation time is restricted to the interval from 0.01 ms to 1.58 ms. However, when the water content exceeds w_{opt}, the maximum T_2 relaxation time extends to 2.1 ms. The relaxation time, which correlates with the pore radius, is plotted on the x-axis, while the NMR signal intensity (proportional to the water content for each pore diameter) is then plotted on the y-axis. The surface relaxivity coefficient (ρ) is first calculated by Eq. (8) and then substituted into Eq. (5) to obtain the water distribution curves at different compaction water contents (Fig. 8b). The results show that the water distribution curves of all samples appear as unimodal and are mainly distributed in the range of 0.3–300 μm. The peak areas in the samples increase gradually as the water content increases. It is evident that at low compaction water contents (i.e. lower than w_{opt}), the NMR signal intensity appears only between pore diameters of 0.3 μm and 14.9 μm, regardless of the water content in each pore class. In contrast, a non-null NMR signal intensity appears between 14.9 μm and 22.6 μm only when the water content exceeds w_{opt}.

This experimental evidence suggests that when the water content exceeds w_{opt}, the state of water distribution in the as-compacted material changes. This can be related to the fact that

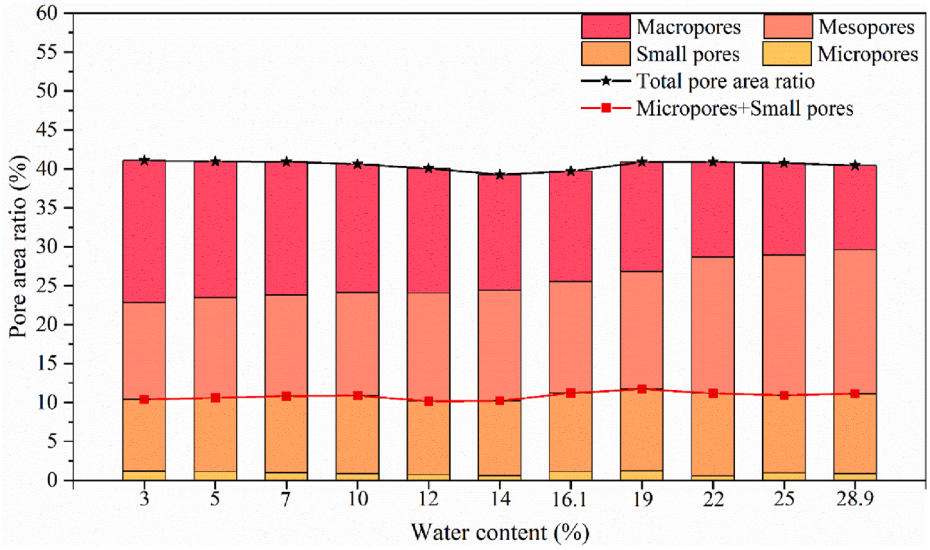

Fig. 7. Pore area ratio variations with compaction water content.

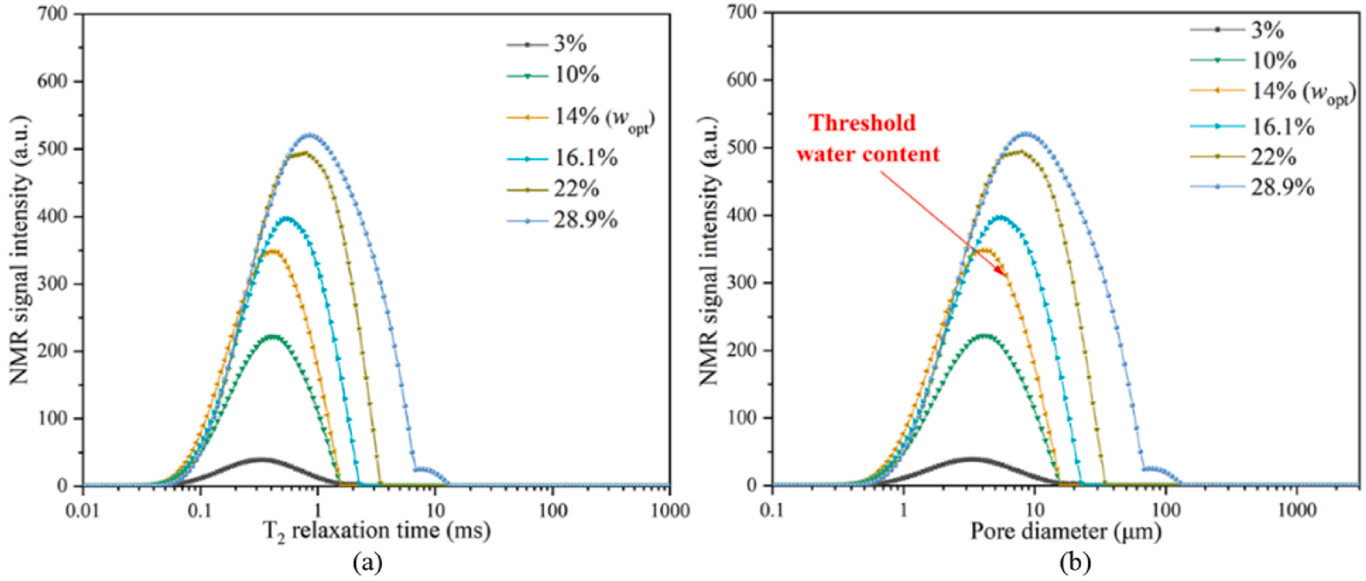

Fig. 8. Water distribution curves for different water contents: (a) T_2 distribution; and (b) Pore diameter.

inter-aggregate water begins to exist. This interpretation regarding the existence of a T_2 threshold between intra- and inter-aggregate water incorporates the methodology proposed by Tian et al. (2018) and Ma et al. (2020), which relies on the evidence that the capillary water-dominated stage (when the soil is wet) and bond water-dominated stage (when the soil is dry) can be identified. The authors performed a series of drying tests and NMR measurements on three soils. In all cases, the right branch of the T_2 distribution curve shifted towards shorter relaxation times with increasing matric suction (i.e. decreasing water content). In particular, the larger T_2 content showed a faster decrease at the beginning of the drying process up to the threshold value of the matric suction. For larger values of matric suction, the maximum value of T_2 remained constant. Since the drying processes considered were driven by changes in the matrix suction imposed by the axis translation technique (i.e. by increasing the air pressure), the disappearance of the T_2 content was essentially related by the authors to the free water, i.e. the water that can be expelled from the porous medium due to the application of a hydraulic gradient. Conversely, the part of the T_2 content that is insensitive to the applied matric suction was related to the bound water. Based on this methodology, the critical gravimetric water content acting as a limit value for intra-aggregate water can be considered equal to 14%, corresponding to w_{opt}.

However, determining the critical threshold between intra- and inter-aggregate water in unsaturated soil mechanics remains a significant challenge. In order to validate the proposed interpretation, a widely accepted approach using the so-called 'residual suction value', derived from the evolution of the soil water retention curve (SWRC) with void ratio, is applied. Using the SWRC data published by Yuan et al. (2024), which were derived from the same loess material used in this study, the residual water content was determined according to the methodology proposed by Vanapalli et al. (1999) and Fredlund and Xing (1994). The

determination procedure involved identifying the residual water content as the intersection between the tangent to the SWRC at the inflection point and the line obtained by following the linear portion of the SWRC at high suction to lower suctions. It is worth noting that the procedure was applied in the semilogarithmic plane ($\log_{10}$(suction) vs. gravimetric water content). Although the SWRC data provided by Yuan et al. (2024) do not span the full suction range suggested for the application of the Vanapalli et al. (1999) procedure, the gravimetric residual water content was estimated to be approximately 13%, which is consistent with the discriminating water content of 14% determined from the NMR data. Although this threshold water content seems to exceed the values reported by Ng et al. (2016) and Wang et al. (2021a) for other loess materials, this difference can be justified by considering that the activity of the studied material is higher than that of the loess studied by the mentioned authors and by recognizing the role of activity on the water retention properties and water distribution (e.g. Skempton, 1953; Mitchell and Soga, 2005; Romero et al., 2011; Della Vecchia et al., 2015).

The threshold water content of approximately 13% obtained from the interpretation of the SWRC data is similar to that obtained by NMR data. Furthermore, considering the changes in hydraulic conductivity and compression behavior described in Sections 4.1 and 4.2 (indicating a transition in mechanical and hydraulic response at a water content of 14%), a w value corresponding to approximately 14% can be considered as the threshold water content discriminating between intra- and inter-aggregate water for the studied loess compacted at a dry density of 1.55 Mg/m^3. The identified value of water content was obtained by comparing a comprehensive set of experimental evidence, at both the microscopic and the laboratory scale, including material stiffness, hydraulic conductivity, and water retention curve.

5. Discussion

The previous sections have highlighted the role of the optimum water content as obtained by the modified Proctor compaction and have shown its basic function as a threshold compaction water content even for statically compacted loess. The hydromechanical behavior of compacted loess depends on several factors, including the compaction water content, the current water content, the proportion of intra- and inter-aggregate water, and the microstructural characteristics, among others. The clay fraction is also expected to exert a pronounced influence on both the water distribution and the hydromechanical properties of loess due to its adsorption capacity, which increases the water retention capacity of loess and its adhesive properties, which promote the binding of soil particles into larger aggregates.

The experimental data presented in Section 4 show that the initial saturated hydraulic conductivity decreases from 2.2×10^{-7} m/s to 8.4×10^{-8} m/s with increasing compaction water content. This trend emphasized the significant influence of the compaction water content on the hydraulic conductivity of compacted loess (Chen et al., 2023b). This is mainly due to differences in water distribution and microstructure caused by the compaction process. Morphological analysis of loess compacted at 3% water content reveals distinct aggregates along with numerous inter-aggregate pores, as shown in Fig. 6. Samples with the lowest water content have the highest initial saturated hydraulic conductivity. As the compaction water content increases, particle aggregates form stronger bonds. Once the compaction water content exceeds the optimum level, inter-aggregate water begins to appear within the sample. This phenomenon is likely related to the migration of clay particles to the surfaces of the aggregates during compaction, resulting in a reduction in the size of larger inter-aggregate pores, as discussed in Section 4.4. When the water content reaches saturation, the aggregated structure of the loess is lost, and the pore connectivity is reduced (Xu et al., 2022). The observed negative correlation between compaction water content and initial saturated hydraulic conductivity can therefore be attributed to the influence of inter-aggregate water during the compaction process. The increase in intra-aggregate water during compaction mainly increases the pore volume filling due to the increase in aggregate size, which is not very susceptible to flow due to the hydraulic gradient. In contrast, the presence of more inter-aggregate water during compaction promotes the movement of clay particles to fill the macropores, resulting in a decrease in the initial hydraulic conductivity. As expected (e.g. Musso et al., 2013; Romero, 2013), an increase in the macropore fraction provides better access to water flow, and thus the macropore area ratio is positively correlated with the initial hydraulic conductivity.

In addition, the saturated hydraulic conductivity evolves with the seepage time, with different trends depending on the compaction water content (Fig. 4a). For samples with low water content, only stable intra-aggregate water is present after compaction. During seepage, the flow of water can induce the movement of clay particles, which can in turn modify the internal microstructure of the loess, potentially blocking the effective seepage channels and inducing a significant decrease in permeability over time. When compacted at a water content greater than the optimum one, the as-compacted samples contain not only intra-aggregate water but also inter-aggregate water, which can contribute to the movement of clay particles during compaction, associated with the formation of weak bonds and a flocculated fabric. As suggested by Wang et al. (2021b), in this case, seepage forces may have facilitated the conversion of weakly bound intra-aggregate water to water susceptible to flow and to the development of a larger pore size (Xu et al., 2021), resulting in an increase in hydraulic conductivity with seepage time.

Regarding the mechanical response, the experimental data clearly show that the preconsolidation pressure (expressed in terms of total vertical stress) decreases with increasing water content, while the compression index gradually increases. Since the test was performed under unsaturated conditions, the results are in line with expectations due to the higher matric suction, driven by interparticle capillary forces, which dominate at lower water contents. However, the distribution of water within the samples plays a critical role. At water contents below the optimum level, most of the water is within the aggregates and has a minimal effect on the compressibility of the material. As water begins to occupy the inter-aggregate voids, matric suction decreases and cementation bonds are weakened, leading to a more pronounced effect of water content on loess compressibility.

6. Conclusions

This paper presents an innovative study of compacted loess, focusing on its hydromechanical properties and microstructural behavior. The significance of this study lies in its comprehensive investigation over a wide range of water contents, from dry to near-saturated conditions, which has not been extensively investigated before. The study provides a consistent framework to link the evidence at the microstructural scale with some evidence at the phenomenological scale. The saturated hydraulic conductivity and unsaturated compression properties of a compacted loess, which has been compacted at different water contents from near-dry to saturated conditions, were investigated using permeability tests and oedometer tests. The permeability test results show that the initial saturated hydraulic conductivity decreases with increasing water content. For compacted loess with water content

below the optimum, the saturated hydraulic conductivity decreases with time. As expected, the unsaturated compressibility increases with increasing water content, but the increase is almost negligible for samples with compaction water content below the optimum. ESEM and NMR tests were performed to explain the changes in hydraulic conductivity and compression behavior of the compacted loess from a microstructural point of view. Using IPP software to quantify the microstructure of the loess, a decrease in the macropore area ratio and a concomitant increase in the mesopore area ratio were found with increasing compaction water content. Finally, quantification of intra- and inter-aggregate water at different compaction water contents using NMR showed that the threshold water content for the presence or absence of inter-aggregate water was close to the optimum one, as determined by the modified Proctor compaction test.

The study's pertinence is further underscored by the significance of permeability and compression properties on the hydro-mechanical behavior of loess for engineering applications (Ying et al., 2021b; Bhukya et al., 2023), including foundation design, soil conservation and flood control, and drainage. The Loess Plateau, due to its vast geographical extent, is geologically divided into three belts: the sandy loess belt, the silty loess belt, and the clayey loess belt, running from north to south. Of these, the silty loess belt occupies the largest area (Cai, 2001; Gao et al., 2021). The loess samples utilized in this study were collected from the Yan'an region of the Loess Plateau in China. These samples, classified as sandy clayey silt, are representative of the silty loess belt (Gao et al., 2021). Consequently, the results of this study are applicable to silty loess throughout the Loess Plateau and potentially to similar regions. The broad applicability provides valuable insights and practical recommendations for construction practices and engineering design in such environments. However, it is imperative to recognize certain limitations in the application of the results of this study to the sandy and clay loess belts, as quantitative extrapolations to loess belonging to a different specific geological context may be inappropriate.

CRediT authorship contribution statement

Kangze Yuan: Writing – review & editing, Writing – original draft, Investigation. **Wankui Ni:** Writing – review & editing, Supervision. **Xiangfei Lü:** Software, Resources. **Haiman Wang:** Investigation. **Yongpeng Nie:** Investigation. **Gabriele Della Vecchia:** Writing – review & editing, Writing – original draft, Supervision, Investigation.

Declaration of competing interest

The authors declare that they have no known competing financial interests or personal relationships that could have appeared to influence the work reported in this paper.

Acknowledgments

The authors gratefully acknowledge the China Postdoctoral Science Foundation (Grant No. 2024MD753992), Shaanxi Geotechnical Mechanics and Engineering Young Talent Support Program Project (Grant No. YESS2024005), and the National Natural Science Foundation of China (Grant No. 41931285).

References

Alonso, E.E., Gens, A., Josa, A., 1990. A constitutive model for partially saturated soils. Geotechnique 40 (2), 405–430.
ASTM D1557–00, 2000. Standard Test Methods for Laboratory Compaction Characteristics of Soil Using Modified Effort. ASTM International, West Conshohocken, USA.
ASTM D1586–08, 2008. Standard Test Method for Standard Penetration Test (SPT) and Split-Barrel Sampling of Soils. ASTM International, West Conshohocken, USA.
ASTM D4318–00, 2000. Standard Test Method for Liquid Limit, Plastic Limit and Plasticity Index of Soils. ASTM International, West Conshohocken, USA.
Atashgahi, S., Tabarsa, A., Shahryari, A., Hosseini, S.S., 2020. Effect of carbonate precipitating bacteria on strength and hydraulic characteristics of loess soil. Bull. Eng. Geol. Environ. 79, 4749–4763.
Bhukya, P.K., Adla, N., Arnepalli, D.N., 2023. Coupled bio-chemo-hydro-mechanical modeling of microbially induced calcite precipitation process considering biomass encapsulation using a micro-scale relationship. J. Rock Mech. Geotech. Eng. 16 (7), 2775–2789.
Cai, Q., 2001. Soil erosion and management on the Loess Plateau. J. Geogr. Sci. 11, 53–70.
Chapuis, R.P., 2012. Predicting the saturated hydraulic conductivity of soils: a review. Bull. Eng. Geol. Environ. 71, 401–434.
Chen, C.L., Jiang, X., Yang, J., 2014. Influence of soil structure on confined compression behaviour of compacted loess. Chin. J. Rock Mech. Eng. 33 (9), 1939–1944 (in Chinese).
Chen, P., Jia, S.G., Wei, X.Q., Sun, P.P., Yi, P.P., Wei, C.F., 2023a. Hydraulic path dependence of shear strength for compacted loess. J. Rock Mech. Geotech. Eng. 15 (7), 1872–1882.
Chen, Z., Kamchoom, V., Chen, R., Prasittisopin, L., 2023b. Investigating the impacts of biochar amendment and soil compaction on unsaturated hydraulic properties of silty sand. Agronomy 13 (7), 1845.
Cheng, K., Heidari, Z., 2017. Combined interpretation of NMR and TGA measurements to quantify the impact of relative humidity on hydration of clay minerals. Appl. Clay Sci. 143, 362–371.
Cui, H.Z., Jin, Z.Y., Bao, X.H., 2018. Effect of carbon fiber and nanosilica on shear properties of silty soil and the mechanisms. Constr. Build. Mater. 189, 286–295.
Damiano, E., Greco, R., Guida, A., Olivares, L., Picarelli, L., 2017. Investigation on rainwater infiltration into layered shallow covers in pyroclastic soils and its effect on slope stability. Eng. Geol. 220, 208–218.
Della Vecchia, G., Dieudonné, A.C., Jommi, C., Charlier, R., 2015. Accounting for evolving pore size distribution in water retention models for compacted clays. Int. J. Numer. Anal. Methods GeoMech. 39 (7), 702–723.
Della Vecchia, G., Jommi, C., Romero, E., 2013. A fully coupled elastic–plastic hydromechanical model for compacted soils accounting for clay activity. Int. J. Numer. Anal. Methods GeoMech. 37 (5), 503–535.
Evstatiev, D., 1988. Loess improvement methods. Eng. Geol. 25, 341–366.
Fredlund, D.G., Xing, A., 1994. Equations for the soil-water characteristic curve. Can. Geotech. J. 31, 521–532.
Gao, C., Xu, L., Coop, M.R., Huang, C., Zuo, L., 2021. An investigation of particle breakage in loess. Eng. Geol. 286, 106083.
GB/T 50123–2019, 2019. Standard for Geotechnical Testing Method. China Planning Press, Beijing, China (in Chinese).
Guo, Y.X., Ni, W.K., Liu, H.S., 2021. Effects of dry density and water content on compressibility and shear strength of loess. Geomech. Eng. 24, 419–430.
Hou, K., Qian, H., Zhang, Q., Lin, T., Chen, Y., Zhang, Y.T., Qu, W.G., 2020. Influence of Quaternary paleoclimate change on the permeability of the loess–paleosol sequence in the Loess Plateau, northern China. Earth Surf. Process. Landf. 45, 862–876.
Hou, X.K., Qi, S.W., Li, Y., Liu, F.C., Li, T.L., Li, H., 2024. Hydraulic conductivity over a wide suction range of loess with different dry densities. J. Rock Mech. Geotech. Eng. 17 (1), 481–492.
Jia, L., Guo, J., Zhou, Z.D., 2019. Experimental investigation on strength development of lime stabilized loess. RSC Adv. 9, 19680–19689.
Kenyon, W.E., Day, P.I., Straley, C., Willemsen, J.F., 1988. A three-part study of NMR longitudinal relaxation properties of water-saturated sandstones. SPE Form. Eval. 3 (3), 622–636.
Kong, L.W., Sayem, H.Md, Tian, H.H., 2018. Influence of drying–wetting cycles on soil-water characteristic curve of undisturbed granite residual soils and microstructure mechanism by nuclear magnetic resonance (NMR) spin-spin relaxation time (T_2) relaxometry. Can. Geotech. J. 55, 208–216.
Lan, H., Zhang, T., Peng, J., et al., 2023. Large scale land reclamation and the effects on hydro-mechanical behavior in loess and loess-derived fill. Eng. Geol. 323, 107241.
Lei, H.Y., Wang, L., Jia, R., Jiang, M.J., Zhang, W.D., Li, C.Y., 2020. Effects of chemical conditions on the engineering properties and microscopic characteristics of Tianjin dredged fill. Eng. Geol. 269, 105548.
Lei, X.Y., 1988. The types of loess pores in China and their relationship with collapsibility. Sci. China, Ser. B 16, 1309–1316.
Leng, Y.Q., Peng, J.B., Wang, Q.Y., Meng, Z.J., Huang, W.L., 2018. A fluidized landslide occurred in the Loess Plateau: a study on loess landslide in South Jingyang tableland. Eng. Geol. 236, 129–136.
Leng, Y.Q., Peng, J.B., Wang, S., Lu, F., 2021. Development of water sensitivity index of loess from its mechanical properties. Eng. Geol. 280, 105918.
Li, P., Pan, Z.D., Xiao, T., Wang, J.D., 2022. Effects of molding water content and compaction degree on the microstructure and permeability of compacted loess. Acta Geotech. 18 (2), 921–936.
Li, P., Vanapalli, S., Li, T.L., 2016. Review of collapse triggering mechanism of collapsible soils due to wetting. J. Rock Mech. Geotech. Eng. 8, 256–274.
Li, X.A., Li, L.C., Song, Y., Hong, B., Wang, L., Sun, J.Q., 2019. Characterization of the

mechanisms underlying loess collapsibility for land-creation project in Shaanxi Province, China – a study from a micro perspective. Eng. Geol. 249, 77–88.
Li, Y., Hou, X.K., Li, T.L., Vanapalli, S.K., Li, P., 2024. Prediction of the hydraulic conductivity function for unsaturated soils over the entire suction range. Can. Geotech. J. https://doi.org/10.1139/cgj-2023-0631.
Li, Y.F., Zhao, C., Li, R., Zhang, H.F., He, Y.Z., Pei, J.Z., Lyu, L., 2025. Dry-process reusing the waste tire rubber and plastic in asphalt: modification mechanism and mechanical properties. Constr. Build. Mater. 458, 139759.
Liu, J.Y., Li, X.A., Xue, Q., Guo, Z.Z., 2020. Experimental study on air permeability and microscopic mechanism of intact and remolded Malan loess, Loess Plateau, China. Bull. Eng. Geol. Environ. 79, 3909–3919.
Luo, H., Wu, F.Q., Chang, J.Y., Xu, J.B., 2018. Microstructural constraints on geotechnical properties of Malan Loess: a case study from Zhaojiaan landslide in Shaanxi Province, China. Eng. Geol. 236, 60–69.
Ma, T.T., Wei, C.F., Yao, C.Q., Yi, P.P., 2020. Microstructural evolution of expansive clay during drying–wetting cycle. Acta Geotech. 15, 2355–2366.
Mitchell, J.K., Soga, K., 2005. Fundamentals of Soil Behavior, third ed. Wiley, New York, USA.
Moore, D.M., Reynolds, R.C.J., 1997. X-Ray Diffraction and the Identification and Analysis of Clay Minerals, second ed. Oxford University Press, Oxford, UK.
Mu, Q.Y., Zhou, C., Ng, C.W.W., 2020. Compression and wetting induced volumetric behavior of loess: macro- and micro-investigations. Transp. Geotech. 23, 100345.
Musso, G., Azizi, A., Jommi, C., 2020. A microstructure-based elastoplastic model to describe the behaviour of a compacted clayey silt in isotropic and triaxial compression. Can. Geotech. J. 57, 1025–1043.
Musso, G., Romero, G., Della Vecchia, G., 2013. Double-structure effects on the chemo-hydro-mechanical behaviour of a compacted active clay. Geotechnique 63 (3), 206–220.
Musso, G., Scelsi, G., Della Vecchia, G., 2024. Chemo-mechanical behaviour of non-expansive clays accounting for salinity effects. Geotechnique 74 (7), 632–646.
Ng, C.W.W., Sadeghi, H., Hossen, S.B., Chiu, C.F., Alonso, E.E., Baghbanrezvan, S., 2016. Water retention and volumetric characteristics of intact and re-compacted loess. Can. Geotech. J. 53 (8), 1258–1269.
Ni, W.K., Yuan, K.Z., Lü, X.F., Yuan, Z.H., 2020. Comparison and quantitative analysis of microstructure parameters between original loess and remoulded loess under different wetting-drying cycles. Sci. Rep. 10, 5547.
Nie, Y.P., Ni, W.K., Lü, X.F., 2024. Effects of dry-wet cycles on compacted loess: from macroscopic to microscopic investigation. Eur. J. Environ. Civ. Eng. 28 (6), 1370–1393.
Peng, J.B., Wang, G.H., Wang, Q.Y., Zhang, F.Y., 2017. Shear wave velocity imaging of landslide debris deposited on an erodible bed and possible movement mechanism for a loess landslide in Jingyang, Xi'an, China. Landslides 14, 1503–1512.
Romero, E., 2013. A microstructural insight into compacted clayey soils and their hydraulic properties. Eng. Geol. 165, 3–19.
Romero, E., Della Vecchia, G., Jommi, C., 2011. An insight into the water retention properties of compacted clayey soils. Geotechnique 61 (4), 313–328.
Scelsi, G., Abed, A.A., Della Vecchia, G., Musso, G., Sołowski, W.T., 2021. Modelling the behaviour of unsaturated non-active clays in saline environment. Eng. Geol. 295, 106441.
Shao, X.X., Zhang, H.Y., Tan, Y., 2018. Collapse behavior and microstructural alteration of remolded loess under graded wetting tests. Eng. Geol. 233, 11–22.
Shepard, F.P., 1954. Nomenclature based on sand-silt-clay ratios. J. Sediment. Res. 24 (3), 151–158.
Skempton, A.W., 1953. Soil mechanics in relation to geology. Proc. Yorks. Geol. Soc. 29 (1), 33–62.
Sun, L., Li, P., Xiao, T., Wang, J., 2023. Influence of compaction condition on the UCS and structure of compacted loess. Environ. Earth Sci. 82, 411.
Tian, H.H., Wei, C.F., Wei, H.Z., Yan, R.T., Chen, P., 2014. An NMR-based analysis of soil–water characteristics. Appl. Magn. Reson. 45, 49–61.
Tian, H.H., Wei, C.F., Lai, Y., Chen, P., 2018. Quantification of water content during freeze–thaw cycles: a nuclear magnetic resonance based method. Vadose Zone J. 17, 1–12.
Vanapalli, S.K., Fredlund, D.G., Pufahl, D.E., 1999. The influence of soil structure and stress history on the soil–water characteristics of a compacted till. Geotechnique 49, 143–159.
Wang, H.M., Liao, D., Ni, W.K., Yuan, K.Z., Ren, S.Y., Guo, Y.X., 2025. New insights and modeling of the evolution of loess infiltration characteristics under multiple rainfalls induced by climate on the Loess Plateau of China. Eng. Geol. 344, 107858.
Wang, H.M., Ni, W.K., Yuan, K.Z., Li, L., Nie, Y.P., Guo, Y.X., 2021b. Microstructure evolution of loess under multiple collapsibility based on nuclear magnetic resonance and scanning electron microscopy. J. Mt. Sci. 18, 2612–2625.
Wang, Y., Li, T.L., Zhao, C.X., Hou, X.K., Li, P., Zhang, Y.G., 2021a. A study on the effect of pore and particle distributions on the soil water characteristic curve of compacted loess soil. Environ. Earth Sci. 80, 764.
Xie, W.L., Li, P., Zhang, M., 2018. Collapse behavior and microstructural evolution of loess soils from the Loess Plateau of China. J. Mt. Sci. 15 (8), 1642–1657.
Xiong, K., Zhang, J.P., He, Y.Z., Li, J.B., Zhang, M.L., Li, R., Lyu, L., 2024. Introducing the mineral powder to strengthen polyurethane grouting materials for crack repair of asphalt pavements. Constr. Build. Mater. 453, 139023.
Xu, P., Qian, H., Zhang, Q.Y., Shang, J.T., Guo, Y., Li, M.N., 2022. Response mechanism of permeability change of remolded loess to seepage parameters. J. Hydrol. 612, 128224.
Xu, P., Zhang, Q.Y., Qian, H., Li, M., Yang, F., 2021. An investigation into the relationship between saturated permeability and microstructure of remolded loess: a case study from Chinese Loess Plateau. Geoderma 382, 114774.
Xu, P., Zhang, Q.Y., Qian, H., Qu, W., 2020. Effect of sodium chloride concentration on saturated permeability of remolded loess. Minerals 10, 199.
Ying, Z., Cui, Y.J., Benahmed, N., Duc, M., 2021a. Changes of small strain shear modulus and microstructure for a lime-treated silt subjected to wetting-drying cycles. Eng. Geol. 293, 106334.
Ying, Z., Cui, Y.J., Benahmed, N., Duc, M., 2021b. Salinity effect on the compaction behaviour, matric suction, stiffness and microstructure of a silty soil. J. Rock Mech. Geotech. Eng. 13, 855–863.
Ying, Z., Cui, Y.J., Benahmed, N., Duc, M., 2023. Drying effect on the microstructure of compacted salted silt. Geotechnique 73, 62–70.
Yu, B., Liu, G.H., Liu, Q.S., Huang, C., Li, H., Zhao, Z.H., 2019. Seasonal variation of deep soil moisture under different land uses on the semi-arid Loess Plateau of China. J. Soils Sediments 19, 1179–1189.
Yuan, K.Z., Ni, W.K., Lü, X.F., Wang, X.J., 2021. Permeability characteristics and structural evolution of compacted loess under different dry densities and wetting-drying cycles. PLoS One 16, e0253508.
Yuan, K.Z., Li, Q.X., Ni, W.K., Lü, X.F., Della Vecchia, G., Wang, H.M., Nie, Y., 2023. Analysis of the structural and environmental impacts of hydrophilic ZSM-5 molecular sieve on loess. Constr. Build. Mater. 366, 130248.
Yuan, K.Z., Ni, W.K., Della Vecchia, G., Lü, X.F., Wang, H.M., Nie, Y.P., 2024. Influence of dry density and wetting–drying cycles on the soil–water retention curve of compacted loess: experimental data and modeling. Acta Geotech. 19, 8111–8128.
Yuan, K.Z., Ni, W.K., Lü, X.F., Della Vecchia, G., Wang, H.M., Li, L., Nie, Y.P., 2022. Influence of wetting–drying cycles on the compression behavior of a compacted loess from microstructure analysis. Bull. Eng. Geol. Environ. 81, 348.
Zhang, M., Liu, J., 2010. Controlling factors of loess landslides in western China. Environ. Earth Sci. 59, 1671–1680.
Zhuang, J.Q., Peng, J.B., Wang, G., et al., 2017. Prediction of rainfall-induced shallow landslides in the Loess Plateau, Yan'an, China, using the TRIGRS model. Earth Surf. Process. Landf. 42, 915–927.

Dr. Kangze Yuan is a lecturer and postdoctoral researcher at Northwest University, China. He obtained his PhD degree from Chang'an University, China, in 2023 and conducted a two-year academic visit at Politecnico di Milano in Italy during his PhD studies. His current research interests focus on the physical and mechanical properties of improved loess and the microstructural mechanisms underlying these improvements. To date, he has authored or co-authored over 30 academic publications and is the principal investigator of a project funded by the China Postdoctoral Science Foundation.